Solar Phys (2014) 289:319–338
DOI 10.1007/s11207-013-0319-3

Simulated (STEREO) Views of the Solar Wind Disturbances Following the Coronal Mass Ejections of 1 August 2010

Y. Zhang · A.M. Du · X.S. Feng · W. Sun · Y.D. Liu · C.D. Fry · C.S. Deehr · M. Dryer · B. Zieger · Y.Q. Xie

Received: 26 June 2012 / Accepted: 3 May 2013 / Published online: 8 June 2013

Abstract Images observed by the twin spacecraft *Solar TErrestrial RElations Observatory* (STEREO) A and B appear as complex structures for two coronal mass ejections (CMEs) on 1 August 2010. Therefore, a series of sky maps of Thomson-scattered white light by interplanetary coronal mass ejections (ICMEs) on 1 August 2010 are simulated using the Hakamada–Akasofu–Fry (HAF) three-dimensional solar-wind model. A comparison between the simulated images and observations of STEREO-A and -B clarifies the structure

Y. Zhang (✉) · A.M. Du
Institute of Geology and Geophysics, Chinese Academy of Sciences, Beijing 100029, China
e-mail: yzhang@mail.iggcas.ac.cn

A.M. Du
e-mail: amdu@mail.iggcas.ac.cn

X.S. Feng · Y.D. Liu
State Key Laboratory of Space Weather, National Space Science Center, Chinese Academy of Sciences, Beijing, China

X.S. Feng
e-mail: fengx@spaceweather.ac.cn

Y.D. Liu
e-mail: liuxying@ssl.berkeley.edu

W. Sun · C.S. Deehr
Geophysical Institute, University of Alaska, Fairbanks, AK 99775-7320, USA

W. Sun
e-mail: wsun_1939@yahoo.com

C.S. Deehr
e-mail: cdeehr@gi.alaska.edu

Y.D. Liu
Space Sciences Laboratory, University of California, Berkeley, CA 94720, USA

C.D. Fry
Exploration Physics International, Inc, Huntsville, AL 35806, USA
e-mail: gfry@expi.com

and evolution of ICMEs (including shocks) in the observed images. The results demonstrate that the simulated images from the HAF model are very useful in the interpretation of the observed images when the ICMEs overlap within the fields of view of the instruments onboard STEREO-A and -B.

1. Introduction

It is well known that large solar flares and coronal mass ejections (CMEs) are drivers of major space-weather effects. They are responsible for the most intense solar energetic-particle events and cause major geomagnetic storms in the terrestrial environment. Although CMEs have been studied by many solar and space scientists, our knowledge about their physical characteristics remains limited.

White-light coronagraphs and heliospheric imagers are used for imaging observations of CMEs. The *Solar and Heliospheric Observatory* (SOHO)/*Large Angle and Spectrometric Coronagraph* (LASCO) can detect CMEs and observe their propagation. However, the upper limit of the field of view (FOV) of the LASCO instrument is only 32 solar radii ($R_\odot$). Starting in 2003, images of CMEs have been made farther from the Sun by the *Solar Mass Ejection Imager* (SMEI) on the *Coriolis* spacecraft. SMEI consists of three wide-angle, white-light, CCD cameras and it has an all-sky FOV of $> 20°$ (Jackson *et al.*, 2004). However, there is still a gap of around 45 $R_\odot$ between the outer edge of the LASCO FOV and the inner edge of SMEI. The launch of the *Solar TErrestrial RElations Observatory* (STEREO) in 2006 provided an opportunity to overcome this problem. STEREO consists of two spacecraft, each almost sharing the same orbit around the Sun as that of the Earth. STEREO-A (A = Ahead of Earth) is moving faster and is slightly closer to the Sun than the Earth, while STEREO-B (B = Behind) is a little farther from the Sun and trailing the Earth; the angular separation between each spacecraft and the Earth increases by about 22.5° per year (Kaiser *et al.*, 2008). The *Sun Earth Connection Coronal and Heliospheric Investigation* (SECCHI) instrument array onboard STEREO is composed of five imaging telescopes including an extreme ultraviolet imager (EUVI), two coronagraphs (COR1, 2), and two heliospheric imagers (HI-1, 2). The EUVI instrument obtains full-disk solar images in four extreme ultraviolet (EUV) wavelengths, producing images with a cadence as rapid as 2.5 minutes (Howard *et al.*, 2008). The COR1 instrument has an FOV of $1.5 – 4.0$ $R_\odot$ and COR2 has an FOV of $2.5 – 15$ $R_\odot$. HI-1 has an FOV of $4° – 24°$and HI-2 has an FOV of $19° – 89°$.

Together, all of these instruments can track a CME from the solar corona to 1 AU and beyond. Therefore, the SECCHI instrument suite provides continuous observations of CMEs

M. Dryer
Space Weather Prediction Center, Ret., National Oceanic and Atmospheric Administration, Boulder, CO 80305, USA
e-mail: Murray.Dryer@msn.com

B. Zieger
Center for Space Physics, Boston University, 725 Commonwealth Ave, Boston, MA 02215, USA
e-mail: berci@bu.edu

Y.Q. Xie
College of Meteorology and Oceanography, PLA University of Science and Technology, Nanjing 211101, China
e-mail: yqxie@spaceweather.ac.cn

from the Sun to the Earth (Howard *et al.*, 2008). The STEREO spacecraft have great potential to enhance the quality of space-weather predictions, because density structures can be tracked on their way to Earth beyond the LASCO FOV (Zhao *et al.*, 2010; Liu *et al.* 2010a, 2010b, 2011; Temmer *et al.*, 2012). However, one of the difficulties associated with the interpretation of the SECCHI observations is how to distinguish different types of density structures in the heliosphere (Lugaz, Vourlidas, and Roussev, 2009). Simulations by a physical model could be used to overcome this problem by creating synthetic line-of-sight images that can be directly compared with heliospheric image observations (Manchester *et al.*, 2008). This could improve our understanding of CMEs/interplanetary (ICMEs).

Recently, a number of three-dimensional (3D) solar-wind models have been developed and used to study these observed ICMEs for both scientific and operational purposes. These models include those based on the 3D magnetohydrodynamic (MHD) models (see, *e.g.*, Groth *et al.*, 2000; Odstrcil, Riley, and Zhao, 2004; Tóth *et al.*, 2005; Feng, Zhou, and Wu, 2007; Wu *et al.*, 2007; Riley *et al.*, 2008; Feng *et al.*, 2010; Wu *et al.*, 2011; Odstrcil *et al.*, 2013). Unfortunately, few of these models run fast enough, even on large computers, to facilitate real-time space-weather forecasts. The Hakamada–Akasofu–Fry (HAF) model, on the other hand, is a 3D kinematic solar-wind model that can quickly provide a description of the background solar wind as well as shocks generated by solar events, based on solar observations (Hakamada and Akasofu, 1982; Fry, 1985; Sun *et al.*, 1985; Akasofu, 2001). This kinematic model has demonstrated its value in the study of the solar-wind macro-scale structure and the investigation of propagation of disturbances in interplanetary space. Using this model, statistical results for shock arrival times have been made for the rising phase of Solar Cycle 23 by Fry *et al.* (2003), for the maximum phase by McKenna-Lawlor *et al.* (2006), and for the declining phase by Smith *et al.* (2009). An extensive set of real-time studies has also been made during Solar Cycle 23 for special epochs by Sun *et al.* (2002a, 2002b) and Dryer *et al.* (2004). In the work of Sun *et al.* (2003), the interplanetary shock waves were projected onto the plane of the sky so that they could guide the interpretation of interplanetary scintillation (IPS) observations, or other observations of line-of-sight (LOS) density. Using the HAF model, Sun *et al.* (2008) simulated the SMEI observations of a halo CME on 27 – 29 May 2003, and the SMEI images have confirmed that these simulations of the ICME geometry are reasonably accurate (Howard *et al.*, 2007; Webb *et al.*, 2009).

In this article, we show that simulations of a series of solar events allow us to sort out the interplanetary density structures from these events that overlap within the FOVs of the observing instruments. In this process, the time-dependent, 3D structure of particle density, calculated using the HAF model, is converted to Thomson-scattered white-light intensity and compared to photometric observations of eruptive ejecta and shocks made by the twin STEREO spacecraft A and B. In Section 2, STEREO observations of the solar events of 1 August 2010 are described in detail. In Section 3, the HAF model is briefly introduced and simulations of solar-wind parameters at the Earth and STEREO-A and -B are presented. The propagation of the multiple and merging CME/shocks in the ecliptic plane is shown, and the transformation of Thomson-scattered light from the CME event is presented. In Section 4, comparisons between the synthetic LOS images and the STEREO-A and -B observations are given. Our discussion and conclusions are presented in Section 5.

2. Observations

On 1 August 2010, STEREO-A and -B were located at N05W78 and S02E71 in heliographic coordinates, respectively. The two spacecraft were separated by about 149° in longitude.

NASA's *Solar Dynamics Observatory* (SDO)/*Atmospheric Imaging Assembly* (AIA) instruments revealed that two filament-eruption events occurred on 1 August 2010 (Schrijver and Title, 2011). The two filaments were associated with two separate CMEs. The two CMEs were first seen in STEREO/COR1 images at about 0242 UT and 0748 UT, respectively (Liu *et al.*, 2012). As reported by the NOAA/Space Weather Prediction Center, a C3.2 X-ray flare associated with the second CME occurred at 0755 UT on 1 August, 2010 from active region AR 11092, which was located at N20E36. The first filament eruption occurred at about 0240 UT from the active region AR 11094, leading AR 11092 by about 25°, and the second one, centered near N37W32, began to rise at about 0630 UT (Schrijver and Title, 2011).

The HI-A telescopes view to the East (left) of the Sun–spacecraft line, while the HI-B telescopes view to the western (right) half. As an example, the top two panels in Figure 1 display the images of the CMEs from the HI-1 onboard STEREO-A at 1729 UT, 1 August and those on STEREO-B at 0409 UT 2 August, respectively. The middle two panels show those from the HI-2 instruments on STEREO-A at 0609 UT 2 August and those on STEREO-B at 0610 UT 2 August, respectively. In order to give a panoramic view of the CME evolution from the low corona to large distances, two overlapping views of the SECCHI telescopes together onboard STEREO-A and -B are shown in the bottom row of Figure 1. The image is a composite of images taken with the COR2, HI-1, and HI-2, right to left for STEREO-A and left to right for STEREO-B. The propagation of the CMEs can be observed from COR2 to HI-1 and from HI-1 to HI-2. The locations of Earth, Venus, and Jupiter are also indicated.

3. HAF Simulations

3.1. Input Parameters for HAF Model

The HAF model has two components: background solar wind and event-driven solar wind. The background solar wind is established by the inner boundary conditions. The coronal magnetic field and the outflow of plasma establish the ambient solar-wind structure. Observations by various solar observatories of LOS photospheric magnetic fields are individually combined to construct daily and synoptic magnetogram maps of the radial magnetic field. The velocity at the source surface at 2.5 $R_\odot$ is computed using the Wang–Sheeley–Arge (WSA) algorithm (Wang and Sheeley, 1990; Wang *et al.*, 1997; Arge and Pizzo, 2000).

3.1.1. Source Surface Map

We note that the coronal magnetic field and velocity on the source surface in this work are calculated using the background solar-wind model that was developed independently by Yang *et al.* (2011) on the basis of the work of Cohen *et al.* (2007). This model makes use of solar magnetogram data and the WSA model. The initial coronal magnetic field is obtained through the potential field source surface model. The final self-consistently coronal magnetic field (2.5 $R_\odot$) is then obtained by solving the MHD equations. The velocity at the source surface at 2.5 $R_\odot$ is computed using the WSA model. Figure 2 shows the simulated solar source-surface velocity and B field at 2.5 $R_\odot$ for Carrington Rotation 2099. The asterisk and triangle symbols indicate the locations of the Earth, STEREO-A and -B, and the two CMEs on 1 August, respectively.

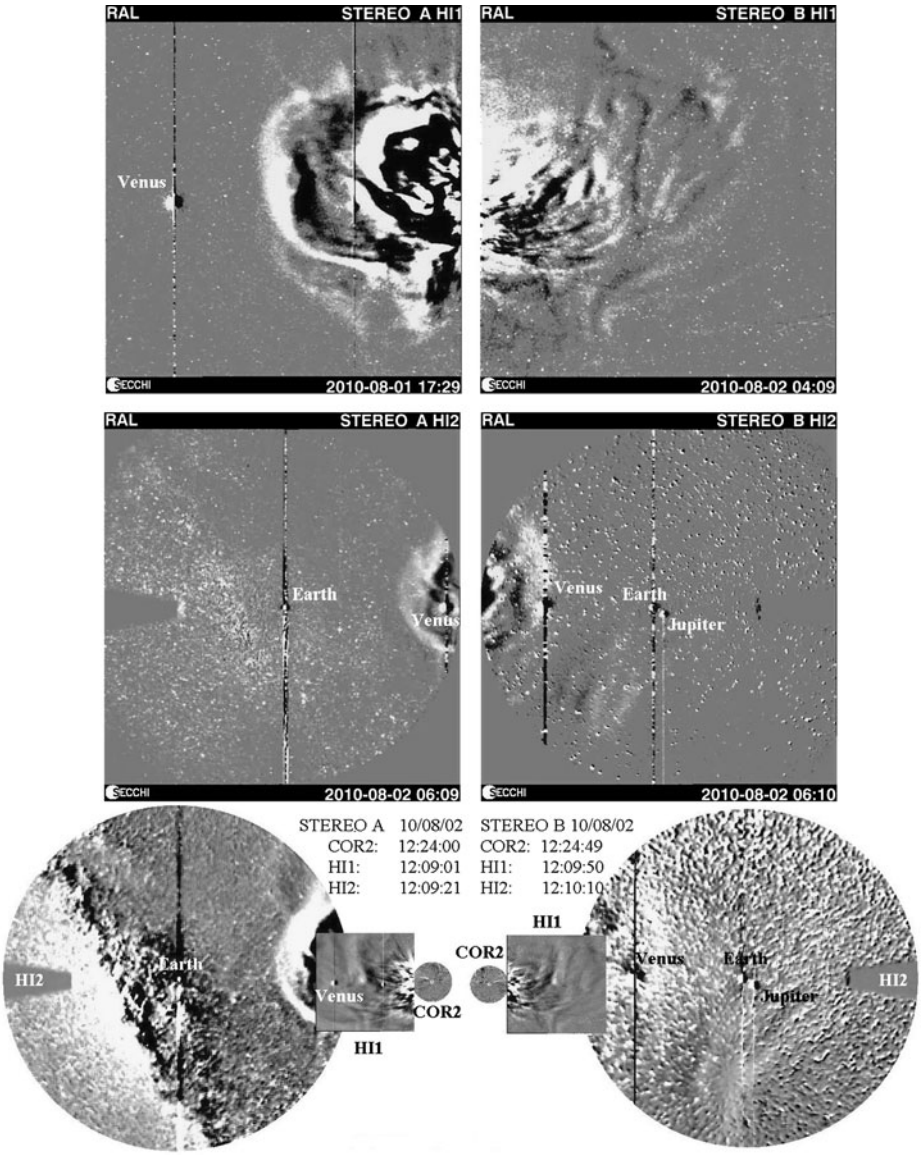

Figure 1 Running-difference images of the August 2010 CMEs observed by STEREO-A (left) and -B (right) near simultaneously. The top row displays HI-1 images with FOVs of 4 – 24° from STEREO-A and -B, respectively. The middle row shows images from HI-2 with FOVs of 19 – 89°. The bottom row shows the overlap views of the SECCHI telescopes. The image is a composite of images taken with COR2, HI-1, and HI-2. COR2 has a FOV of 0.7 – 4°. The positions of the Earth, Venus, and Jupiter are also indicated.

3.1.2. The Event-Driven Components

Solar observations provide the start time, location, and magnitude for the solar eruption source. The solar event is represented by time-dependent boundary conditions at the source surface (at 2.5 $R_{\odot}$). The disturbance energy is characterized by the enhanced solar wind on

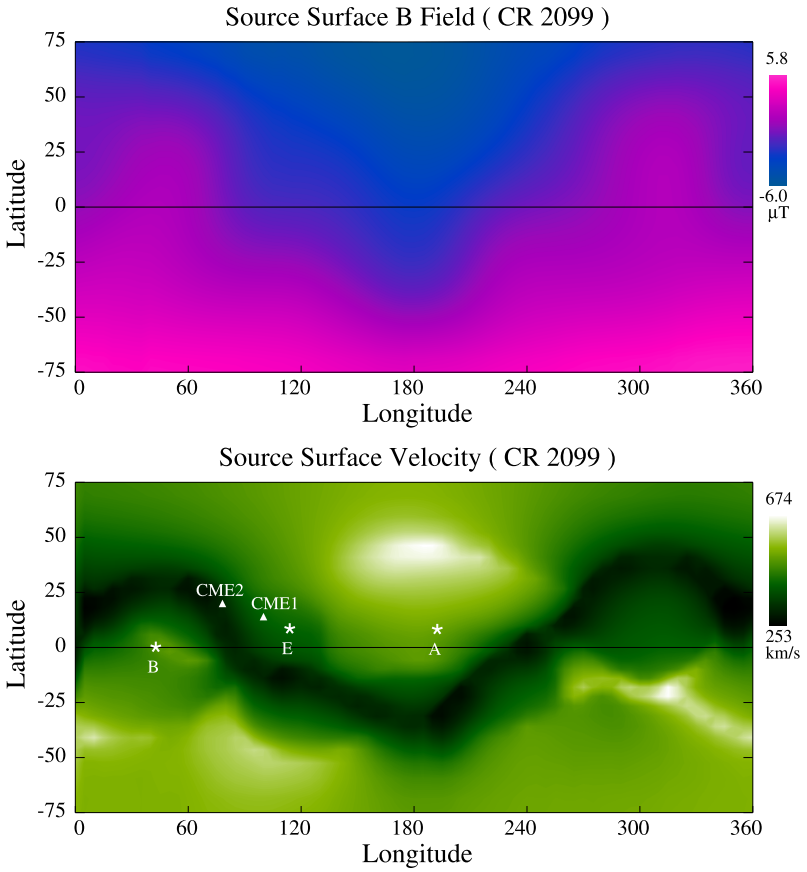

Figure 2 Synoptic plot of the radial magnetic fields and velocities at the source surface (2.5 $R_\odot$), as obtained from the Yang *et al.* (2011) and WSA model based on the LOS photospheric magnetic-field observations at Wilcox Solar Observatory for Carrington Rotation 2099. The asterisk and triangle symbols indicate the locations of Earth, STEREO-A and -B, and the two CMEs considered here on 1 August 2010.

Table 1 Solar events of 1 August 2010[a].

Supporting solar observations									Observed arrivals			
Events	Year	M	D	UT_1	V_{CME}, $km\,s^{-1}$	Location	τ, h	CME	S/C	M	D	UT_2
CME0	2010	07	30	0730	540	N16E58	6.25	Partial Halo				
CME1	2010	08	01	0242	730	N14E14	1.5	Partial Halo	W	08	03	1704
CME2	2010	08	01	0748	1 140	N20E36	3.5	Halo	W	08	03	1704

[a] V_{CME} is the speed of CME. τ is piston driving duration, estimated by using X-ray flare duration as proxy; S/C is spacecraft data used, where W is Wind. UT_1 is the launch time of the CME.

the source surface. The input data and the observed shock arrival times are shown in Table 1 (see also Schrijver and Title (2011) and Liu *et al.* (2012), for an expanded version of the first part of this table).

When the HAF model is operated for real-time forecast, the initial speed is usually estimated from the metric type II radio-burst speed, or, if no metric radio type II bursts observations were available, the CME speed can be measured from imager data. In this work, we use the CME speed as the initial speed. We considered that the two CMEs on 1 August would be interacting with the background solar wind and the preceding CME (Liu *et al.*, 2012). Therefore, the CME of 30 July 2010, labeled as CME0, is included as an input event to the HAF model. This CME is launched at about 0730 UT on 30 July with a speed around 540 km s^{-1}. The speeds of the two CMEs on 1 August, labeled as CME1-2, are about 730 km s^{-1} and 1140 km s^{-1}, respectively. The speeds are obtained from linear fits to CME propagation distances before CME collisions (Liu *et al.*, 2012).

The start times of the events were determined by the launch times of the CMEs, which are estimated by extrapolating the coronagraph observations of SECCHI back to the solar surfaces (Liu *et al.*, 2012). The piston driving time [τ] is provided by the *Geostationary Operational Environmental Satellite* (GOES)-7 soft X-ray duration. The τ-parameter is the difference in time between the rise time of the integrated X-ray flux and the time of its decrease, measured linearly on the logarithmic flux scale at a level set at half the distance from the background level to the peak (Fry *et al.*, 2001).

Because the two eruptions were only four hours apart and CME2 was faster than CME1, the two CMEs merged quickly and the front of the merged structures is likely a shock wave (Liu *et al.*, 2012). The combined shock associated with the two CMEs arrived at the Earth at 1704 UT on 3 August 2010, as observed by the *Wind* spacecraft. Using the HAF model, this shock was predicted to arrive at 1700 UT on 3 August 2010. The simulation results are shown in Figure 3 and will be discussed in Section 3.2. It can be seen that the simulation is in reasonably good agreement with the observations at the *Wind* spacecraft, as well as with those of STEREO-B.

3.2. Simulation of Solar Wind Parameters

Ecliptic-plane plots (prepared in real time) of a snapshot of interplanetary magnetic field at six different times from 1 to 5 August are shown in Figure 3. The red lines are field lines directed away from the Sun, and blue represents field lines directed toward the Sun. The Earth's location is indicated by the large black dot and labeled "E". The STEREO spacecraft are labeled "A" and "B" at $+78°$ and $-71°$ from the Earth. The edges of the FOVs are indicated as green lines. As shown in Figure 3, it can be seen that the first shock driven by CME0 was predicted to arrive at STEREO-B at about 1400 UT on 2 August. A combined shock, formed from the interaction between CME1 and CME2, was predicted to arrive at STEREO-B at about 0500 UT on 3 August, and then at the Earth at about 1700 UT on 3 August 2010. Note that CME0 was overtaken by the merged front of CME1 and CME2 and merged into one front at its western flank.

The simulation results for the events on 1 August 2010 using the HAF model are shown in Figure 4. From the top to the bottom of Figure 4(a) the solar-wind speed, particle density, and dynamic pressure observed by STEREO-B are shown as a function of time at 1 AU during 1 – 10 August 2010. The HAF simulations are shown by the red curves and the observations by the STEREO-B data in black dots. It can be seen that a shock driven by CME0 was first predicted to arrive at STEREO-B at 1400 UT on 2 August (indicated by the vertical dotted line), and then a merged shock driven by CME1 and CME2 disturbances was predicted to arrive at 0500 UT on 3 August (indicated by the vertical dashed line). Figure 4(b) displays the solar wind plasma parameters at L_1 observed by *Wind* and simulated by the HAF model. The merged shock reached *Wind* at the time indicated by the blue vertical dashed line, and

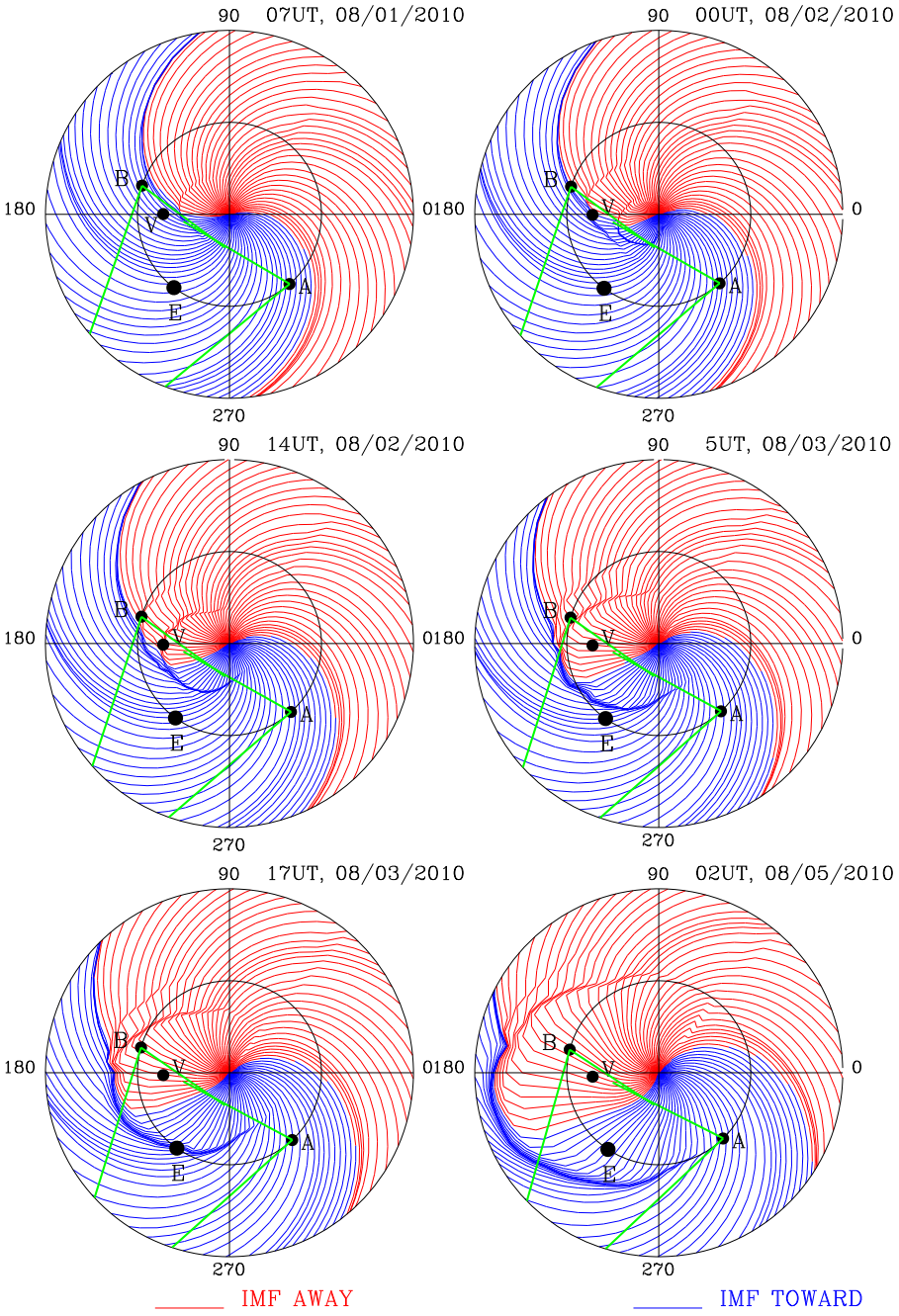

Figure 3 Simulated solar equatorial IMF lines projected on the ecliptic plane to 2 AU as a function of heliographic longitude at six different times during 1 – 5 August 2010. The red color indicates IMF lines directed away from the Sun, and the blue color indicates IMF directed toward the Sun. The large dot shows the location of Earth. STEREO spacecraft are labeled A and B at $+78^\circ$ and -71° from the Earth. The edges of the FOV of HI-2 are indicated as green lines. The location of Venus (labeled by V) is also indicated by a large dot.

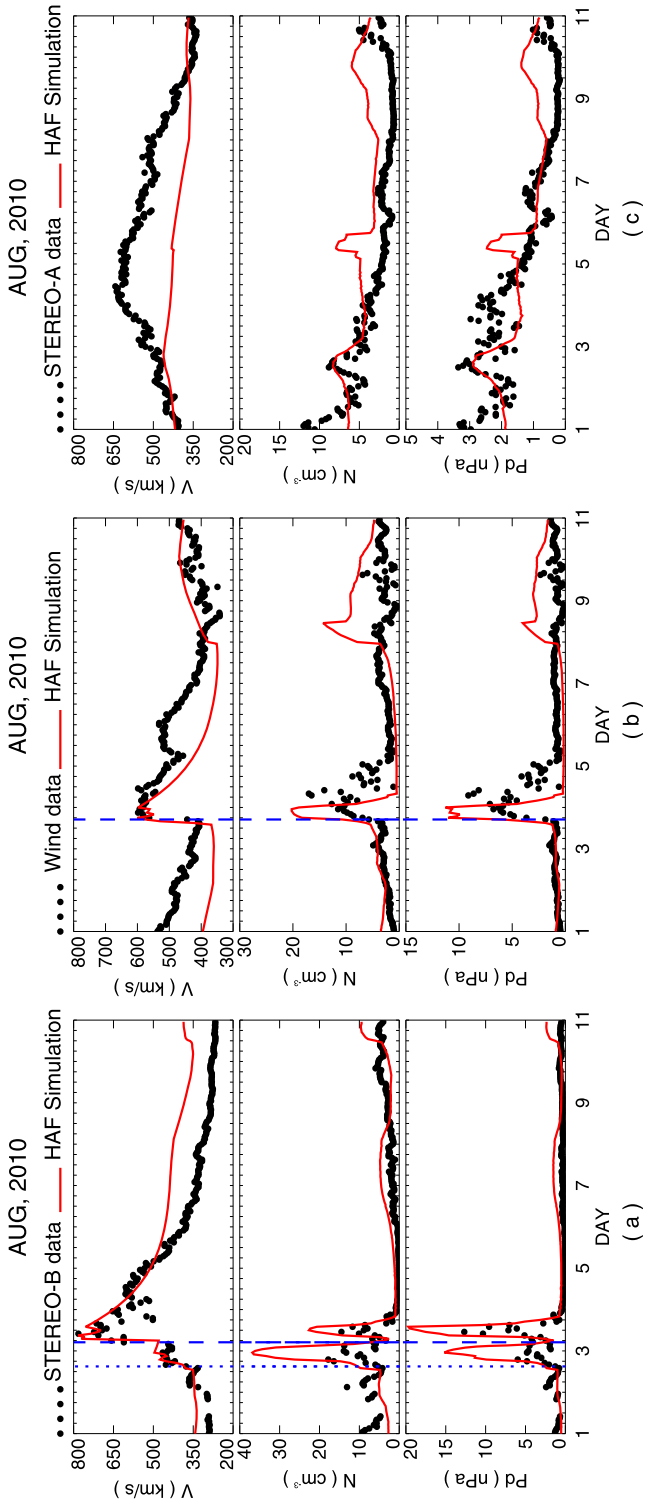

Figure 4 From top to bottom: the solar-wind speed, particle density, and dynamic pressure observed at STEREO-B, Wind, and STEREO-A are shown as a function of time at 1 AU during 1 – 10 August 2010. The red curves are the simulation results using the HAF solar-wind model, and the black dots show the observation results.

arrived at the Earth at 1704 UT on August 3. Figure 4(c) shows that no obvious ICME signatures were observed by STEREO-A during this time interval. The HAF model also suggests that the flank of the combined shock might have been very weak when it reached STEREO-A. Therefore, no evidence of any shock or ejecta signatures at STEREO-A is shown. It is likely that the shock missed STEREO-A because the longitudinal extent of the merged front of CMEs was not large enough to reach it. However, there are slight jumps in simulated density and dynamic pressure at 0200 UT on 5 August, which might be the results of the sweeping of the western flank of the shock. The mimicked initial condition probably results in this overexpansion of the shock shape. Also, the velocity observed by STEREO seems higher than that from the simulation. This might be explained by the unrealistic steady state inner boundary conditions of the HAF model, which is limited by the potential-field assumption in the WSA model.

It can be seen that the merged shock driven by CME1 and CME2 was first observed by STEREO-B, and later by *Wind*. A possible explanation is that CME0 may have removed some of the solar-wind plasma via expansion or rarefaction following the shock/CME0 compression ahead of the CME1/CME2 shock because the former's propagation direction was east of the latter shock (Liu *et al.*, 2012). These results are generally consistent with the observations and interpretations of Liu *et al.* (2012).

Although the simulated arrival times of shocks are roughly consistent with the observation, there are some disagreements. In the case of *Wind*, the velocity and density perturbations following the shock-front arrival seem to be broader (spanning more time) than the results from the simulations. Moreover, the density shock predicted by the model seems to be much steeper than the one measured by *Wind*. This might be caused by an unrealistic shock thickness owing to the unrealistic CME initiation mechanism. As a kinematic solar wind model, the HAF model concerns mainly shock arrival time and shock intensity for time-series output and shock arrival location and shock-front shape for 2D plots in the ecliptic plane. Therefore, the comparison between simulation results and observations would not cover all physical characteristics of shocks (for example, quasi-perpendicular shocks that are examined by particle-in-cell simulations). This might also be the reason why the simulated density of the first ejection is much higher than that of the observed one at STEREO-B.

3.3. Sky Map of the Thomson-Scattered Light

The simulated sky maps of Thomson-scattered white-light intensity are made by calculating the integrated density of solar plasma along the LOSs (Sun *et al.* 2003, 2008) and then converting to scattered white-light radiation to facilitate comparison with the STEREO observations.

Thomson scattering has a strong angular dependence, such that scattering into a LOS is highly dependent on the location of the electron relative to the Sun and the observer (Billings, 1966; Hundhausen, 1993). Close to the Sun, the scattering is heavily weighted to the plane of the sky. At large elongation, the spherical shape of the maximum scattering surface becomes significant to the appearance of white-light images (Vourlidas and Howard, 2006). The scattering is peaked on the Thomson surface, a 0.5 AU radius sphere with a diameter passing through both the Sun and the observer. The Thomson-scattering integral along LOSs from the observer to infinity can be written as (Howard and Tappin, 2009; Tappin and Howard, 2009)

$$I = \int_0^\infty N_e(r) z^2 I_{\text{tot}} \, \mathrm{d}z, \tag{1}$$

where z is the distance of the scattering point from the observer. $N_e(r)$ is the solar-wind electron density at a distance r from the Sun; its value is determined by the particle density of solar-wind plasma. $I_{\rm tot}$ is the total radiation scattered by an electron toward the observer, including two components: transverse and radial. The expression is described as (Billings, 1966; Hundhausen, 1993)

$$I_{\rm tot} = 2I_0 \frac{\pi \sigma_{\rm e}}{2z^2} \sin^2 \chi \big[(1-u)C + uD\big] - I_0 \frac{\pi \sigma_{\rm e}}{2z^2} \sin^2 \chi \big[(1-u)A + uB\big], \tag{2}$$

where I_0 is the integrated scattering radiation per unit area per unit solid angle from the solar surface, $\sigma_{\rm e}$ is the electron-scattering cross section, χ is the angle between the radius through the scattering point and the LOS, and u is an empirical constant (0.56). The coefficients A, B, C, and D are functions of Ω, which is the angle between the radius through the scattering point and the tangent from the scattering point to the solar photosphere:

$$A = \cos\Omega \sin^2\Omega, \tag{3}$$

$$B = -\frac{1}{8}\left[1 - 3\sin^2\Omega - \frac{\cos^2\Omega}{\sin\Omega}\big(1 + 3\sin^2\Omega\big)\ln\left(\frac{1+\sin\Omega}{\cos\Omega}\right)\right], \tag{4}$$

$$C = \frac{4}{3} - \cos\Omega - \frac{\cos^3\Omega}{3}, \tag{5}$$

$$D = \frac{1}{8}\left[5 + \sin^3\Omega - \frac{\cos^2\Omega}{\sin\Omega}\big(5 - \sin^2\Omega\big)\ln\left(\frac{1+\sin\Omega}{\cos\Omega}\right)\right]. \tag{6}$$

The integration is carried out through a conceptual grid in spherical coordinates with a resolution of 0.02 AU $\times$ 4° $\times$ 2° (radius $\times$ longitude $\times$ latitude), with the observer in the center.

4. Comparison of STEREO and HAF Images

4.1. Comparison of STEREO-B and HAF Images

The simulated sky maps at 0800, 1200, 1600, and 2000 UT on 2 August 2010 are shown in the right column of Figure 5. The sky maps are Hammer–Aitoff projections in ecliptic coordinates with longitude extending from −180° to 180° and latitude from −90° to 90°, with the Sun centered at 0°. The HI-1B and HI-2B telescope FOVs (red oval and green oval) are superimposed on the synthetic images. The positions of the Earth and Venus are indicated by green dots. For comparison, the corresponding observations by STEREO-B are shown in the left column of Figure 5. There are bright fronts, indicated by yellow arrows, moving across the field of HI-2B. In each simulated image, there are two arcs of density enhancement within the HI-2B FOV. From the relative positions of the Earth and Venus, we can deduce that the brightness enhancement pointed to by the yellow arrow corresponds to the smaller arc in the synthesized image.

In the right panels of Figure 6, the density structures in the ecliptic plane at the same time sequence as in Figure 5 are given to facilitate interpretation of the white-light images. The intersection of the Thomson sphere with the ecliptic plane is marked with a white circle (right column). As can be seen in these images, the CME0 was compressed by the merged disturbance of CME1 and CME2 at the western flank and finally merged into one front in the field of HI-2B. In order to better compare specific features, in the left panels of Figure 6, we show the simulated images from the same point of view (POV) of HI-2B. It is found that there are two bright structures associated with the two different disturbances. The smaller

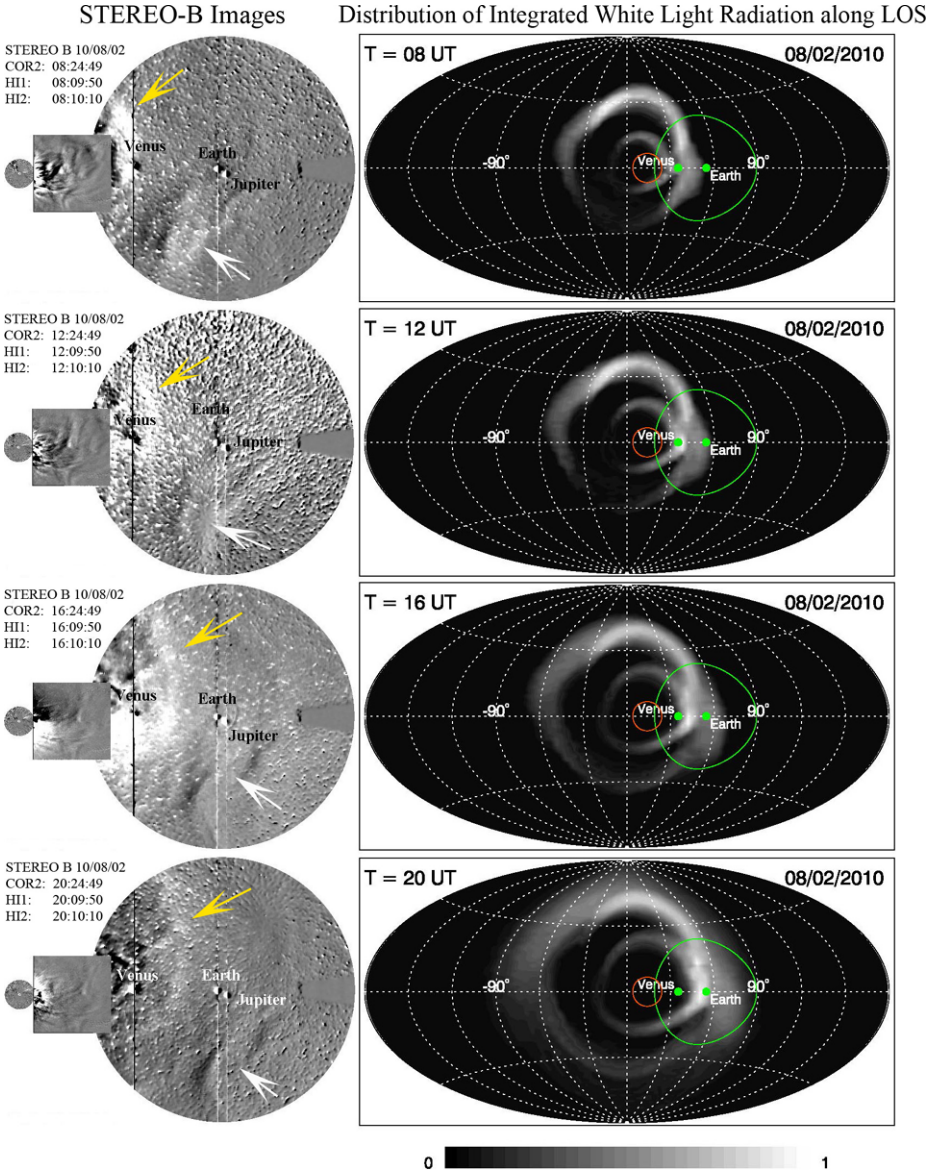

Figure 5 Four of the composite images that were observed by STEREO-B (left) at 0800, 1200, 1600, and 2000 UT on 2 August 2010. The CMEs are shown in a time series propagating through the FOV of COR2, HI-1B, and HI-2B (from left to right) that extend from 0.7° to 4°, 4° to 24°, and 19° to 89° elongation. The position of the Earth, Venus, and Jupiter are also indicated. Also shown are the simulated sky maps (right) in ecliptic coordinates (Hammer–Aitoff projection) at the same time. The HI-1B and HI-2B telescope FOVs (red oval and green oval) are superimposed onto the simulated images. The Earth and Venus are indicated by green points. The location of the CME0 front is indicated by the white arrow, while that of the merged front formed from the interaction between CME1 and CME2 is indicated by the yellow arrow.

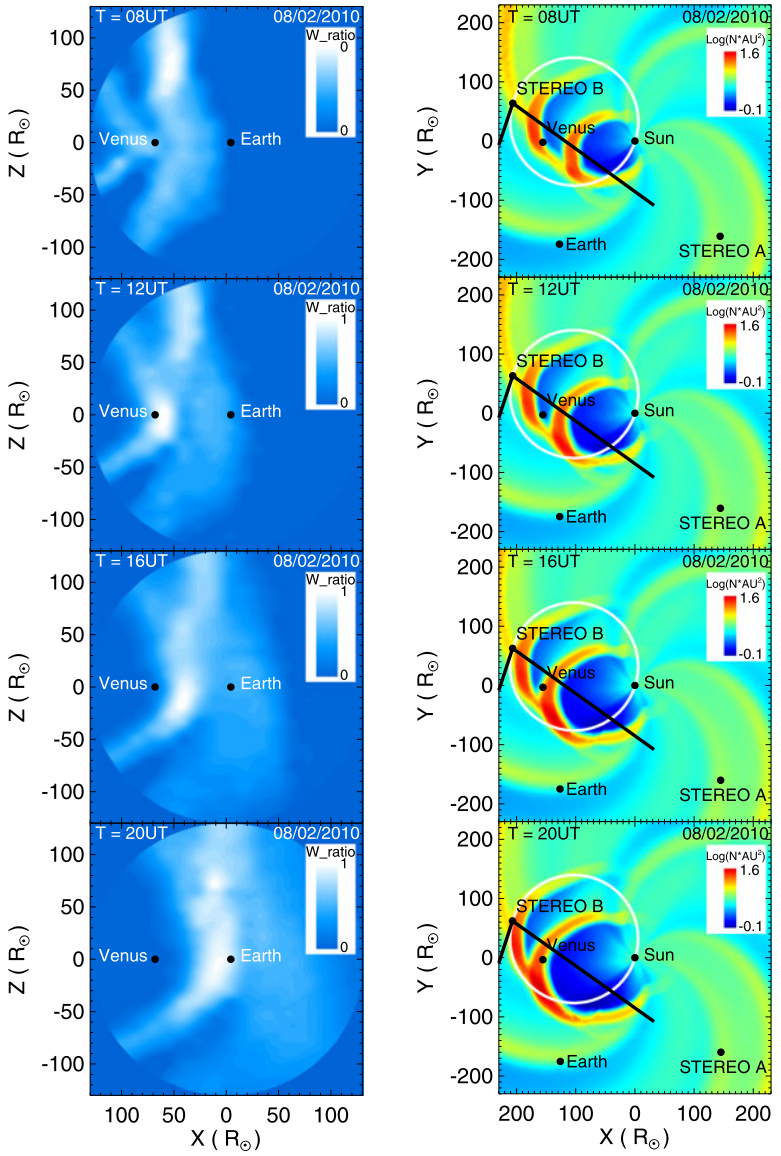

Figure 6 (Left) The simulated SECCHI HI-2B images at the same times as in Figure 5. (Right) Ecliptic plane plots of the predicted proton density (normalized as shown in the color bar). The Sun, Earth, and STEREO-A and -B are shown by the black dots. The white circle is the approximate projection of the Thomson sphere onto the plane of the image. The edges of the FOV of HI-2B are indicated with black lines.

dense arc continues to be brighter because it corresponds to the merged front that is crossing the Thomson surface. The larger arc seems relatively fainter because it corresponds to the CME0 whose integral density along the LOS is much lower than that of the merged CMEs.

Furthermore, the northern part of the larger dense arc seems much brighter than the southern part. The all-sky maps simulated by the HAF model, which can track the front of the CME disturbance as it extends beyond the FOV of SECCHI, help us to interpret

the northerly front. From the simulated full-view images, we found that the CME0 extends significantly to the North and then the density peak appears in the northern direction, as shown in the simulated all-sky map and synthetic HI-2B image.

From the real HI-2B images in Figure 5, we can conclude that the bright fronts indicated by the yellow arrows correspond to the merged fronts of CME 1 and CME2. There is a fair agreement between the overall shape and position of the leading edge of the merged CME disturbance in the real and synthetic images. However, the density enhancement of the front of CME0 cannot be readily seen in the HI-2B observed images where the model predicts the larger intense brightness arc. Nevertheless, we can still identify a very dim structure indicated by a white arrow in the southern half of the real HI-2B image at 0800 UT on 2 August. However, the dim structure gradually fades away and becomes a wave-like structure marked by a white arrow. There is a factor that contributes to this. As shown in Figure 4(a), the simulated CME0 would be clearly identified with a particle density approaching 37 cm^{-3}, while from the observation data, the CME0 is about two times less dense (only 20 cm^{-3}) and might be nearly visible. Moreover, the real image does not capture the northerly front that appeared in the simulated image. This might be due to the unrealistic shock shape owing to the mimicked CME initiation mechanism.

4.2. Comparison of STEREO-A and HAF Images

The first two STEREO-A images in the left column of Figure 7 show a bright front (a thin curve), as indicated by a white arrow in the HI-2A view. A brightness structure was also clearly visible in the FOV of HI-2A in the simulated all-sky maps at the same time. The synthetic images from the same POV of HI-2A are presented in the left panels of Figure 8 to make more direct comparisons with the real ones. There is good agreement between the position of the dense front in the real and synthetic images. However, the asymmetric shape of the simulated dense arc is slightly different from the approximately symmetric shape of the real one, and the simulated dense arc seems significantly brighter in the North of the bright structure. These may be due to the northerly extension of the simulated CME0 as mentioned in Section 4.1. From the density maps projected on the ecliptic plane as shown in the right panels of Figure 8, we found that the bright front enters the HI-2A image FOV (in both the observed and synthetic images) at the same time that the CME0 front crosses the HI-A2 FOV limit. Therefore, we believe that the bright arc indicated by the white arrow corresponds to the leading edge of CME0.

In addition, there are two dense arcs in both the observed and synthetic all-sky images. One arc is in the FOV of HI-2A, which corresponds to the leading edge of CME0 and the other is in the FOV of HI-1A, which corresponds to the merged front of CME1 and CME2. The lower three STEREO-A images in the left column of Figure 7 show an extraordinarily bright front (indicated by the yellow arrow) moving across the field of HI-2A, which corresponds to the merged front of CME1 and CME2. The thin curve could not be found in the FOV of the HI-2A image at 1809 UT on 2 August. From the density structure in the Ecliptic in the left panels of Figure 8, it is easily seen that the CME0 structure may have been hidden by the interaction with the merged front of CME1 and CME2. On the other hand, it might have become too faint and no longer visible in the FOV of HI-2A around 1809 UT on 2 August. Therefore, the bright front indicated by the yellow arrow corresponds to the leading edge of the merged front of CME1 and CME2.

We also measured the distance from the Sun of the merged front of CME1 and CME2 as a function of time using the STEREO/COR2, HI-A data, and simulated results. The location of the merged front of CME1 and CME2 as a function of time for the simulation and

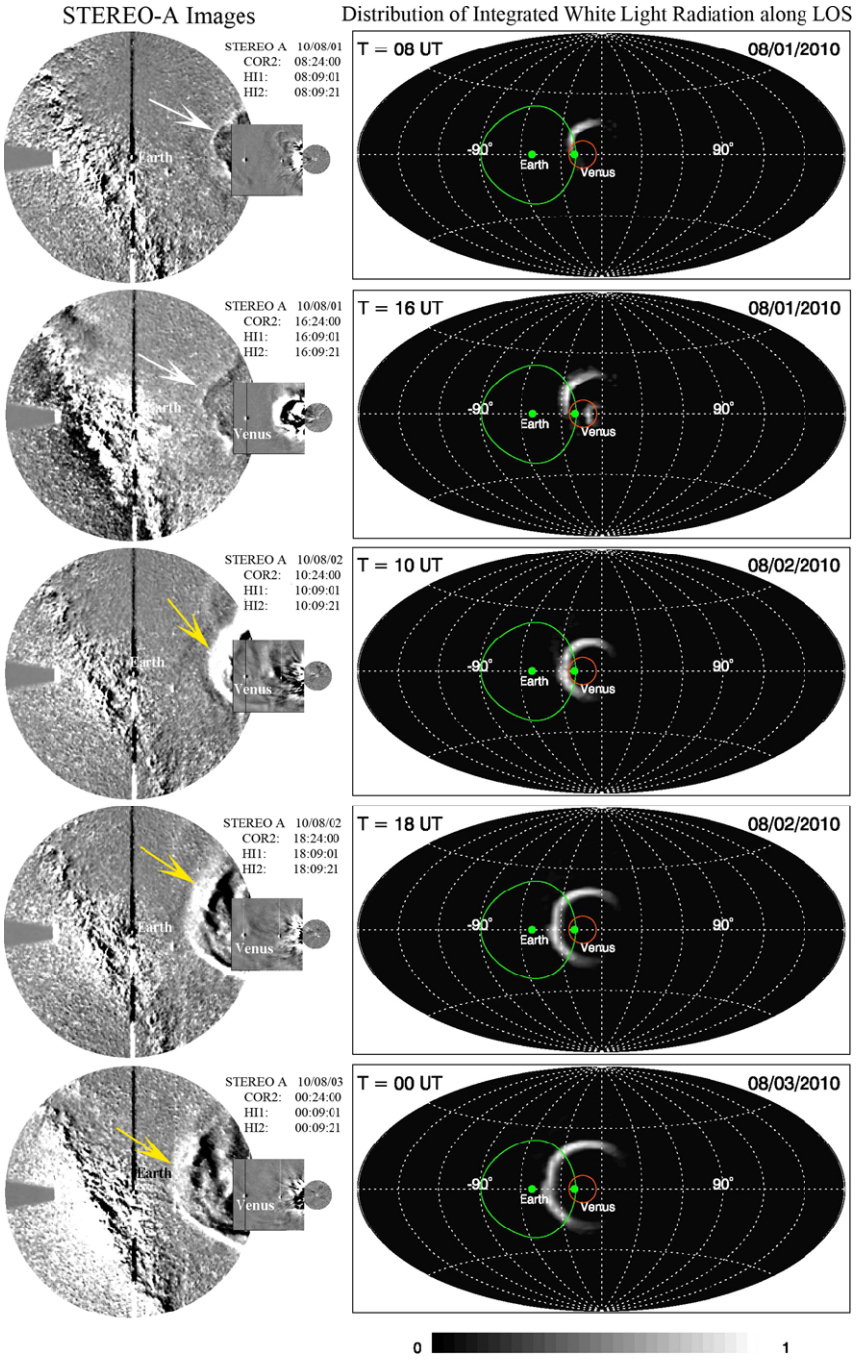

Figure 7 Five of the composite images that were observed by STEREO-A (left) at 0800, 1600 UT on 1 August, at 1000, 1800 UT on 2 August, and at 0000 UT on 3 August 2010. The CMEs are shown in a time series propagating through the FOV of COR2, HI-1A, and HI-2A (from right to left) that extend from 0.7° to 4°, 4° to 24°, and 19° to 89° elongation. Also shown are the simulated sky maps at the same time (right). See Section 4.2 for the implications of this simulation.

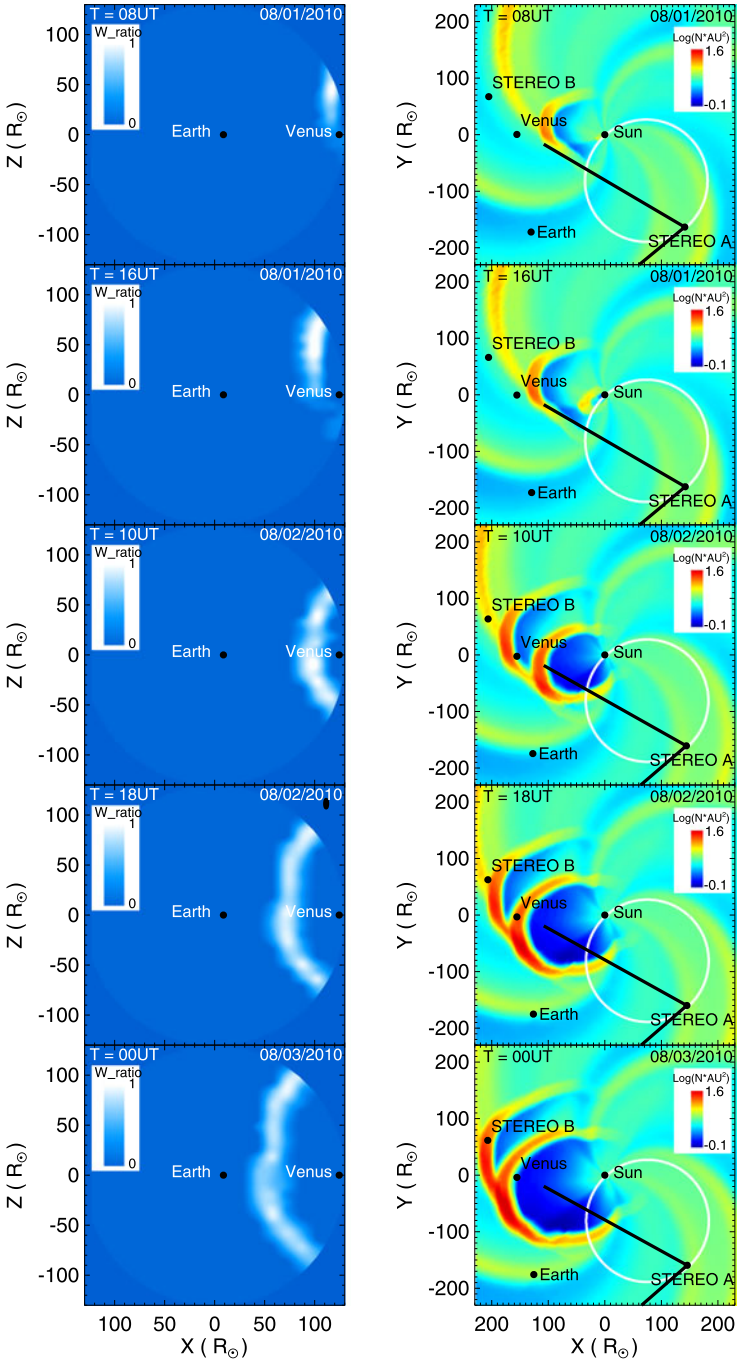

Figure 8 (Left) The simulated SECCHI HI-2A images at the same times shown in Figure 7. (Right) The ecliptic-plane model density maps normalized as indicated in the scale.

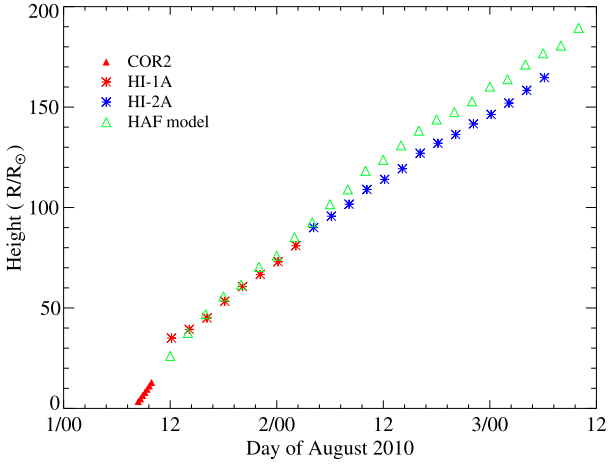

Figure 9 Distance–time curves of the leading edge of ICMEs with the STEREO-A/COR2, HI data and the simulated results of the HAF model.

observations of STEREO-A is shown in Figure 9. It seems that the HAF model's results better match the HI-A data within 100 $R_\odot$ and align with the HI-A data for distances larger than 130 $R_\odot$. We note that the result given by the HAF model appears to be about five hours ahead of the HI-A data at large distances (> 130 $R_\odot$). It is partly caused by an overexpansion of the western flank of the merged shock driven by CME1 and CME2 as a result of the uncertainty in the simulated shock's width.

5. Discussion and Conclusions

It is obvious that the brightness and structure of a CME observed by STEREO-A and -B along lines of sight depend on the CME's expansion, its distance from the Sun, the observing instrument, and the Thomson surface. The white-light images are affected not only by the geometry of the CME, but also by the projection on the plane of the sky. However, simulated sky maps derived from the solar-wind model are useful for identifying CME structures. Also, by obtaining the geometry and trajectory of the structure, simulations are useful for discerning different CMEs.

In this article, we have simulated sky maps of Thomson-scattered white light of the two CMEs that occurred on 1 August 2010 using the HAF model and have made detailed comparisons of these images with those made by STEREO-A and -B. It is demonstrated that the simulated sky maps are in good agreement with the images observed by STEREO for the events. Both events were located between the line connecting the Sun and STEREO-A and the line connecting the Sun and STEREO-B. The HI-A telescopes only view to the East of the Sun–spacecraft line, while the HI-B telescopes only view the western half. Therefore, in this case the ICMEs were able to enter the FOVs of both HI-A and HI-B. This facilitates the comparison of the simulation results with the observations from different directions.

Images of STEREO/HI are difficult to interpret, in particular when multiple density structures appear in the FOV of the instrument. The HAF simulation allows us to associate the observed STEREO features with features in the synthetic images and the simulated 2D interplanetary magnetic field (IMF)/density maps on the ecliptic plane. The shock fronts of the ICMEs can be identified. This is an essential point that is often overlooked in space-weather forecasting of what might, metaphorically, be referred to as "tsunami" arrival times.

Of course, we do not address the consequences of associated IMF polarities. Moreover, the HAF model, which can obtain all-sky maps, is helpful in distinguishing which part of the dense arc is moving across the FOV of the real observations by analyzing the dense structure outside the FOV of instruments onboard STEREO-A and -B.

In conclusion, combining observations with model simulations can lead to a better understanding of the structure and propagation of ICMEs. In future work, the comparison of the model with the observation will guide us in adjusting key model parameters such as initial conditions and arrival times, leading to improvements in model performance.

Acknowledgements This work is jointly supported by the National Natural Science Foundation of China (41104093, 41031066, 41174122), and the Chinese Academy of Sciences (KZZD-EW-01-3), the China Postdoctoral Science Foundation. We thank Jih-Kwin Chao and C.B. Wang for providing the HAFv.1 code for our use. C.D. Fry's participation is supported by University of Alabama Huntsville Sub-Award SUB2010-045 under NASA Grant NNX09AP74A. Y.D. Liu is supported by the STEREO project under grant NAS5-03131, by the SPORT project under grant Y129164CBS, by the Recruitment Program of Global Experts of China under grant Y3B0Z1A840, by the Specialized Research Fund for State Key Laboratories of China, and by the CAS/SAFEA International Partnership Program for Creative Research Teams. We are grateful to the SOHO team for the interplanetary shock list. We acknowledge the use of data from SOHO, STEREO, and ACE. We also thank Y.D. Liu for providing the movies on his website. Finally, we express our appreciation to the referee for constructive comments and suggestions.

References

Akasofu, S.I.: 2001, Predicting geomagnetic storms as a space weather project. In: Song, P., Siscoe, G., Singer, H. (eds.) *Geophys. Monagr. Ser.* **125**, AGU, Washington, 329 – 337.

Arge, C.N., Pizzo, V.J.: 2000, Improvement in the prediction of solar wind conditions using near-real-time solar magnetic field updates. *J. Geophys. Res.* **105**, 10465 – 10479. doi:10.1029/1999JA000262.

Billings, D.E.: 1966, *A Guide to the Solar Corona*, Academic Press, New York.

Cohen, O., Sokolov, I.V., Roussev, I.I., Arge, C.N., Manchester, W.B., Gombosi, T.I., Frazin, R.A., Park, H., Butala, M.D., Kamalabadi, F., Velli, M.: 2007, A semi-empirical magnetohydrodynamical model of the solar wind. *Astrophys. J. Lett.* **654**, L163 – L166. doi:10.1086/511154.

Dryer, M., Smith, Z., Fry, C.D., Sun, W., Deehr, C.S., Akasofu, S.I.: 2004, Real-time predictions of interplanetary shock arrivals at L1 during the "Halloween 2003" Epoch. *Space Weather* **2**, S09001. doi:10.1029/2004SW000087.

Feng, X.S., Zhou, Y.F., Wu, S.T.: 2007, A novel numerical implementation for solar wind modeling by the modified conservation element/solution element method. *Astrophys. J.* **655**, 1110 – 1126. doi:10.1086/510121.

Feng, X.S., Yang, L.P., Xiang, C.Q., Wu, S.T., Zhou, Y.F., Zhong, D.K.: 2010, Three-dimensional solar wind modeling from the sun to earth by a SIP-CESE MHD model with a six-component grid. *Astrophys. J.* **723**, 300 – 319. doi:10.1088/0004-637X/723/1/300.

Fry, C.D.: 1985, Three-dimensional structure of the heliosphere: Quiet-time and disturbed periods. Ph.D. Thesis, University of Alaska, Fairbank, AK.

Fry, C.D., Sun, W., Deehr, C.S., Dryer, M., Smith, Z., Akasofu, S.I., Tokumaru, M., Kojima, M.: 2001, Improvements to the HAF solar wind model for space weather predictions. *J. Geophys. Res.* **106**, 20985 – 21002. doi:10.1029/2000JA000220.

Fry, C.D., Dryer, M., Smith, Z., Sun, W., Deehr, C.S., Akasofu, S.I.: 2003, Forecasting solar wind structures and shock arrival times using an ensemble of models. *J. Geophys. Res.* **108**, 1070. doi:10.1029/2002JA009474.

Groth, C.P.T., De Zeeuw, D.L., Gombosi, T.I., Powell, K.G.: 2000, Global three-dimensional MHD simulation of a space 15 weather event: CME formation, interplanetary propagation, and interaction with the magnetosphere. *J. Geophys. Res.* **105**, 25053 – 25078. doi:10.1029/2000JA900093.

Hakamada, K., Akasofu, S.I.: 1982, Simulation of three-dimensional solar wind disturbance and resulting geomagnetic storms. *Space Sci. Rev.* **31**, 3 – 70. doi:10.1007/BF00349000.

Howard, T.A., Tappin, S.J.: 2009, Interplanetary coronal mass ejections observed in the heliosphere: 1. Review of theory. *Space Sci. Rev.* **147**, 31 – 54. doi:10.1007/s11214-009-9542-5.

Howard, T.A., Fry, C.D., Johnston, J.C., Webb, D.F.: 2007, On the evolution of coronal mass ejections in the interplanetary medium. *Astrophys. J.* **667**, 610 – 625. doi:10.1086/519758.

Howard, R.A., Moses, J.D., Vourlidas, A., Newmark, J.S., Socker, D.G., Plunkett, S.P., *et al.*: 2008, Sun earth connection coronal and heliospheric investigation (SECCHI). *Space Sci. Rev.* **136**, 67 – 115. doi:10.1007/s11214-008-9341-4.

Hundhausen, A.J.: 1993, Sizes and locations of coronal mass ejections—SMM observations from 1980 and 1984 – 1989. *J. Geophys. Res.* **98**, 13177 – 13200. doi:10.1029/93JA00157.

Jackson, B.V., Buffington, A., Hick, P.P., Altrock, R.C., Figueroa, S., Holladay, P.E., Johnston, J.C., Kahler, S.W., Mozer, J.B., Price, S., *et al.*: 2004, The solar mass-ejection imager (SMEI) mission. *Solar Phys.* **225**, 177 – 207. doi:10.1007/s11207-004-2766-3.

Kaiser, M.L., Kucera, T.A., Davila, J.M., St. Cyr, O.C., Guhathakurta, M., Cristian, E.: 2008, The STEREO mission: an introduction. *Space Sci. Rev.* **136**, 5 – 16. doi:10.1007/s11214-007-9277-0.

Liu, Y., Davies, J.A., Luhmann, J.G., Vourlidas, A., Bale, S.D., Lin, R.P.: 2010a, Geometric triangulation of imaging observations to track coronal mass ejections continuously out to 1 AU. *Astrophys. J. Lett.* **710**, L82 – L87. doi:10.1088/2041-8205/710/1/L82.

Liu, Y., Thernisien, A., Luhmann, J.G., Vourlidas, A., Davies, J.A., Lin, R.P., Bale, S.D.: 2010b, Reconstructing coronal mass ejections with coordinated imaging and in situ observations: global structure, kinematics, and implications for space weather forecasting. *Astrophys. J.* **722**, 1762 – 1777. doi:10.1088/0004-637X/722/2/1762.

Liu, Y., Luhmann, J.G., Bale, S.D., Lin, R.P.: 2011, Solar source and heliospheric consequences of the 2010 April 3 coronal mass ejection: a comprehensive view. *Astrophys. J.* **734**, 84. doi:10.1088/0004-637X/734/2/84.

Liu, Y.D., Luhmann, J.G., Moestl, C., Martinez-Oliveros, J.C., Bale, S.D., Lin, R.P., Harrison, R.A., Temmer, M., Webb, D.F., Odstrcil, D.: 2012, Interactions between coronal mass ejections viewed in coordinated imaging and in situ observations. *Astrophys. J. Lett.* **746**, L15. doi:10.1088/2041-8205/746/2/L15.

Lugaz, N., Vourlidas, A., Roussev, I.I.: 2009, Deriving the radial distances of wide coronal mass ejections from elongation measurements in the heliosphere – application to CME-CME interaction. *Ann. Geophys.* **27**, 3479 – 3488. doi:10.5194/angeo-27-3479-2009.

Manchester, W.B., Vourlidas, A., Tóth, C., Lugaz, N., Roussev, I.I., Sokolov, I.V., De Zeeuw, D.L., Opher, M.: 2008, Three-dimensional MHD simulation of the 28 October 2003 coronal mass ejection: comparison with LASCO coronagraph observations. *Astrophys. J.* **684**, 1448 – 1460. doi:10.1086/590231.

McKenna-Lawlor, S.M.P., Dryer, M., Kartalev, M.D., Smith, Z., Fry, C.D., Sun, W., Deehr, C.S., Kecskemety, K., Kudela, K.: 2006, Near real-time predictions of the arrival at the earth of flare-generated shocks during solar cycle 23. *J. Geophys. Res.* **111**, A11103. doi:10.1029/2005JA011162.

Odstrcil, D., Riley, P., Zhao, X.P.: 2004, Numerical simulation of the 12 May 1997 interplanetary CME event. *J. Geophys. Res.* **109**, A02116. doi:10.1029/2003JA010135.

Odstrcil, D., Xie, H., de Koning, C.A., Rouillard, A.P., Möstl, C., Jian, L.K., Dryer, M., Davies, J.A., Harrison, R.A., Zhang, T.L.: 2013, Numerical heliospheric simulation as an assisting tool for interpretation of the "first STEREO multi-event", four coronal mass ejections (CMEs) of 2010-08-01. *Astrophys. J.*, in preparation.

Riley, P., Lionello, R., Mikić, Z., Linker, J.: 2008, Using global simulations to relate the three-part structure of coronal mass ejections to in situ signatures. *Astrophys. J.* **672**, 1221 – 1227. doi:10.1086/523893.

Schrijver, C.J., Title, A.M.: 2011, Long-range magnetic coupling between solar flares and coronal mass ejections observed by SDO and STEREO. *J. Geophys. Res.* **116**, A04108. doi:10.1029/2010JA016224.

Smith, Z.K., Dryer, M., McKenna-Lawlor, S.M.P., Fry, C.D., Deehr, C.S., Sun, W.: 2009, Operational validation of HAFv2's predictions of interplanetary shock arrivals at earth: declining phase of solar cycle 23. *J. Geophys. Res.* **114**, A05106. doi:10.1029/2008JA013836.

Sun, W., Akasofu, S.I., Smith, Z.K., Dryer, M.: 1985, Calibration of the kinematic method of studying the solar wind on the basis of a one dimensional MHD solution and a simulation study of the heliosphere between November 22 – December 6. *Planet. Space Sci.* **33**, 933 – 943. 1977. doi:10.1016/0032-0633(85)90107-2.

Sun, W., Dryer, M., Fry, C.D., Deehr, C.S., Smith, Z., Akasofu, S.I., Kartalev, M.D., Grigorov, K.G.: 2002a, Evaluation of solar type II radio burst estimates of initial solar wind shock speed using a kinematic model of the solar wind on the April 2001 solar event swarm. *Geophys. Res. Lett.* **29**, 1171. doi:10.1029/2001GL013659.

Sun, W., Dryer, M., Fry, C.D., Deehr, C.S., Smith, Z., Akasofu, S.I., Kartalev, M.D., Grigorov, K.G.: 2002b, Real-time forecasting of ICME shock arrivals at L1 during the "April fool's day". *Ann. Geophys.* **20**, 937 – 945. Epoch: 28 March – 21 April 2001. doi:10.5194/angeo-20-937-2002.

Sun, W., Deehr, C.S., Fry, C.D., Dryer, M., Smith, Z., Akasofu, S.I.: 2003, Plane-of-sky simulations of interplanetary shock waves. *Geophys. Res. Lett.* **30**, 20. 2044. doi:10.1029/2003GL017574.

Sun, W., Deehr, C.S., Dryer, M., Fry, C.D., Smith, Z.K., Akasofu, S.I.: 2008, Simulated solar mass ejection imager and "solar terrestrial relations observatory-like" views of the solar wind following the solar flares of 27 – 29 May 2003. *Space Weather* **6**, S03006. 2003. doi:10.1029/2006SW000298.

Tappin, S.J., Howard, T.A.: 2009, Interplanetary coronal mass ejections observed in the heliosphere: 2. Model and data comparison. *Space Sci. Rev.* **147**, 55 – 87. doi:10.1007/s11214-009-9550-5.

Temmer, M., Vršnak, B., Rollett, T., Bein, B., de Koning, C.A., Liu, Y., Bosman, E., Davies, J.A., Möstl, C., Žic, T., Veronig, A.M., Bothmer, V., Harrison, R., Nitta, N., Bisi, M., Flor, O., Eastwood, J., Odstrcil, D., Forsyth, R.: 2012, Characteristics of kinematics of a coronal mass ejection during the 2010 August 1 CME-CME interaction event. *Astrophys. J.* **749**, 57. doi:10.1088/0004-637X/749/1/57.

Tóth, G., Sokolov, I.V., Gombosi, T.I., Chesney, D.R., Clauer, C.R., De Zeeuw, D.L., Hansen, K.C., Kane, K.J., Manchester, W.B., Oehmke, R.C., Powell, K.G., Ridley, A.J., Roussev, I.I., Stout, Q.F., Volberg, O., Wolf, R.A., Sazykin, S., Chan, A., Yu, B., Kóta, J.: 2005, Space weather modeling framework: a new tool for the space science community. *J. Geophys. Res.* **110**, A12226. doi:10.1029/2005JA011126.

Vourlidas, A., Howard, R.A.: 2006, The proper treatment of coronal mass ejection brightness: a new methodology and implications for observations. *Astrophys. J.* **642**, 1216 – 1221. doi:10.1086/501122.

Wang, Y.M., Sheeley, N.R. Jr.: 1990, Solar wind speed and coronal flux-tube expansion. *Astrophys. J.* **355**, 726 – 732. doi:10.1086/168805.

Wang, Y.M., Sheeley, N.R. Jr., Phillips, J.L., Goldstein, B.E.: 1997, Solar wind stream interactions and the wind speed-expansion factor relationship. *Astrophys. J. Lett.* **488**, L51 – L54. doi:10.1086/310918.

Webb, D.F., Howard, T.A., Fry, C.D., Kuchar, T.A., Odstrcil, D., Jackson, B.V., Bisi, M.M., Harrison, R.A., Morrill, J.S., Howard, R.A., Johnston, J.C.: 2009, Study of CME propagation in the inner heliosphere: SOHO LASCO, SMEI and STEREO HI observations of the January 2007 events. *Solar Phys.* **256**, 239 – 267. 2007. doi:10.1007/s11207-009-9351-8.

Wu, C.C., Fry, C.D., Dryer, M., Wu, S.T., Thompson, B., Liou, K., Feng, X.S.: 2007, Three-dimensional global simulation of multiple ICME's interaction and propagation from the heliosphere following the 25 – 28 October 2003 solar events. *Adv. Space Res.* **40**, 1827 – 1834. doi:10.1016/j.asr.2007.06.025.

Wu, C.C., Dryer, M., Wu, S.T., Wood, B.E., Fry, C.D., Liou, K., Plunkett, S.: 2011, Global three-dimensional simulation of the interplanetary evolution of the observed geoeffective coronal mass ejection during the epoch 1 – 4 August 2010. *J. Geophys. Res.* **116**, A12103. doi:10.1029/2011JA016947.

Yang, L.P., Feng, X.S., Xiang, C.Q., Jiang, C.W.: 2011, Numerical validation and comparison of three solar wind heating methods by the SIP-CESE MHD model. *Chin. Phys. Lett.* **28**, 039601. doi:10.1088/0256-307X/28/3/039601.

Zhao, X.H., Feng, X.S., Xiang, C.Q., Liu, Y., Li, Z., Zhang, Y., Wu, S.T.: 2010, Multi-spacecraft observations of the 2008 January 2 CME in the inner heliosphere. *Astrophys. J.* **714**(2), 1133 – 1141. doi:10.1088/0004-637X/714/2/1133.